13th ewtec 2019 Proceedings of the 13th European Wave and Tidal Energy Conference 1-6 Sept 2019, Naples, Italy

Experimental results of a self-rectifying impulse axial-flow air turbine with fixed guide-vanes

Ana F.F. Ponte, Ana A.D. Carrelhas, Luís M.C. Gato, João C.C. Henriques, António F.O. Falcão

***Abstract*—The self-rectifying axial-flow impulse turbine is a popular alternative to the Wells turbine for oscillating-water-column wave energy converter applications. For increasing flow rate coefficient, the peak efficiency point is followed by a gradual decline, which contrasts with the sharp drop that characterizes in general the Wells turbines. This allows the turbine to operate at a not-too-bad efficiency even for the large flow rate coefficients that occur in the more energetic sea states. Self-rectifying impulse turbines are known to have a modest peak efficiency due to the inherent misalignment between the flow direction at rotor exit and the inlet angle of the downstream guide-vanes. This introduces large flow blockage and high stagnation pressure losses. The effect of these losses is aggravated when the inlet stator deflection is large as in conventional unidirectional impulse turbine designs. This paper reports the results of the experimental testing of an axial-flow self-rectifying impulse turbine with a conventional single-row and with a new multiple-row guide-vanes system, both designed to produce large deflection at the inlet stator. The new stator design is inspired in the concentric annular row guide-vane design developed for the self-rectifying biradial turbine which has already been numerically and experimentally validated. In the present case, each inlet and exit guide-vane system comprises three guide-vane rows, which enables high flow deflection at the rotor inlet with reduced blockage, smaller stagnation pressure loss at the downstream guide-vane system, and increased efficiency, in comparison with the original design of a single row of guide-vanes on each side of the rotor and high pitch-to-chord ratio vanes. A 0.59 m rotor diameter axial-flow self-rectifying impulse turbine model was constructed and tested at the 55 kW IST variable-flow blow-down test rig under unidirectional steady-state conditions. Measurements of the air pressure head, the pressure difference across the rotor, flow rate, rotational speed, power output and flow traversing upstream and downstream of the rotor allow the performance assessment of the new turbine design and its comparison with the conventional design.**

***Index Terms*—Impulse turbine; self-rectifying air turbine; model testing; experimental results; wave energy; oscillating water column.**

This paper, with ID 1687, has been submitted in the EWTEC 2019 conference track *Grid integration, power take-off and control.* This research was partially supported by FCT (Foundation for Science and Technology), Portugal, through IDMEC (Institute of Mechanical Engineering), under LAETA, project UID/EMS/50022/2019. The forth author was funded by FCT researcher grant No. IF/01457/2014.

A.F.F. Ponte (e-mail: ana.ponte@tecnico.ulisboa.pt), A.A.D. Carrelhas (e-mail: ana.carrelhas@tecnico.ulisboa.pt), L.M.C. Gato (e-mail: luis.gato@tecnico.ulisboa.pt), J.C.C. Henriques (e-mail: joaochenriques@tecnico.ulisboa.pt), and A.F.O. Falcão (e-mail: antonio.falcao@tecnico.ulisboa.pt) are at IDMEC, Instituto Superior Técnico, Universidade de Lisboa, Av. Rovisco Pais, 1049-001 Lisboa, Portugal

I. Introduction

THE oscillating-water-column (OWC) wave energy converter (WEC) has been object of many theoretical and experimental studies, with several prototypes having been deployed and tested under real sea state conditions [1], [2]. In this type of WEC, the energy conversion process comprises three main stages:(1) the hydrodynamic process of energy conversion from the waves to pneumatic energy in the air chamber of the device; (2) the aerodynamic conversion of energy in the air turbine and (3) the conversion of mechanical power at turbine shaft into electrical power in an electrical generator and in a power electronics system.

In stage 2, the alternately positive and negative pressure difference between the air chamber and the atmosphere is to be converted into turbine shaft power. If a rectifying valve system is to be avoided (which is the adopted option in most cases), the flow through the turbine is bidirectional without change in rotational direction. Such turbines are named self-rectifying. Wells and impulse turbines are the most popular self-rectifying turbines.

The Wells turbine was chosen to equip most WECs deployed into the sea (e.g. Mighty Whale, Japan, 1998; Pico plant, Portugal, 1999; Mutriku breakwater plant, Spain, 2011). The Wells turbine is attractive for its conceptual and mechanical simplicity and for its peak efficiency that may reach about 75% in the best low-solidity designs. On the other hand, as the flow rate coefficient increases beyond the best efficiency point, the angle of attack of the flow velocity relative to the rotor blades (shaped as symmetrical aerofoils) reaches a critical point beyond which massive flow separation occurs (aerodynamic stalling), which results in a sharp drop in efficiency to near-zero values. This severely limits the range of efficient operation of Wells turbines and constitutes their main drawback [3], [4].

The self-rectifying axial-flow impulse turbine is a popular alternative to the Wells turbine for oscillating-water-column wave energy converter applications [5]–[7]. For increasing flow rate coefficient, the peak efficiency point is followed by a gradual decline, which contrasts with the sharp drop that characterizes in general the Wells turbines. This allows the turbine to operate at a not-too-bad efficiency even for the large flow rate coefficients that occur in the more energetic sea states. Self-rectifying impulse turbines are known to have a modest peak efficiency due to the inherent misalignment between the flow direction at rotor exit and the inlet angle of the downstream guide-vanes (see Fig. 1). This introduces large flow blockage and high stagnation pressure losses.

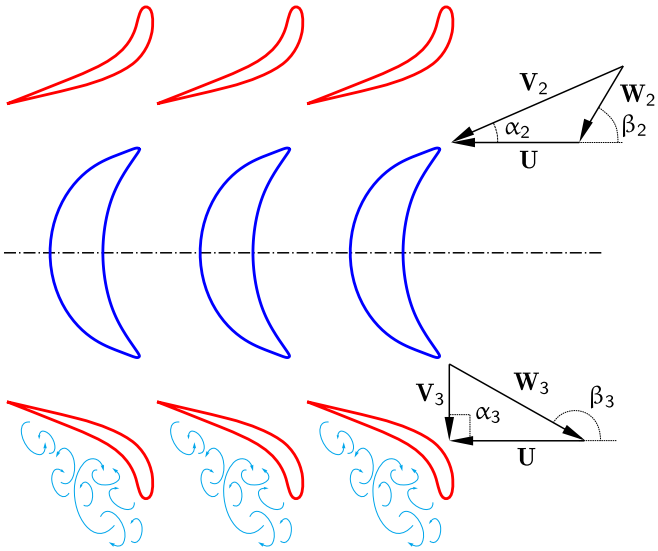

Fig. 1. Guide-vane system of a self-rectifying axial-flow impulse turbine: misalignment between the downstream guide-vanes and the direction of the flow leaving the rotor.

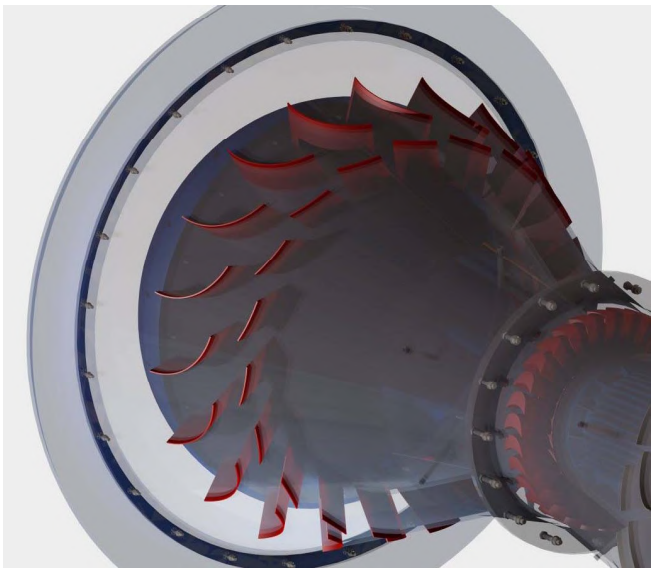

Fig. 2. Schematic representation of the concentric twin guide-vane row topology (reproduced from [12]).

The effect of these losses is aggravated when the inlet guide-vane induced deflection is large as in conventional unidirectional impulse turbine designs.

Previous self-rectifying impulse turbine designs mitigate this problem, either by using movable guide-vanes [8] or by adopting relatively small values for inlet stator absolute flow deflection, corresponding to guide-vane designs with reduced blockage to the rotor exit flow [9]–[11]. However, the latter choice reduces the energy exchange between the rotor and the air-flow, which is detrimental to the turbine efficiency. The measured maximum peak achieved by an axial impulse turbine with fixed guide-vanes is 48% [9]–[11].

The Portuguese company *Kymaner* proposed a new arrangement for the guide-vanes to reduce these losses. It consists in splitting the deflection into two or more rows [12], Fig. 2. This new design ensures the required flow deflection at the rotor inlet, through a parceling

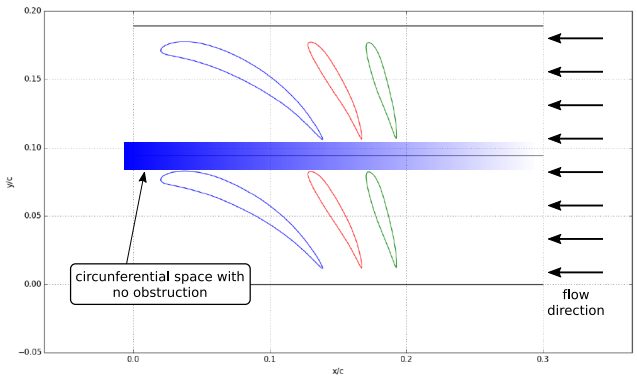

Fig. 3. Representation of the flow leaving the rotor in design conditions and the circumferential space with no obstruction between the guide-vanes for the case of a set of three guide-vane rows.

of the aerodynamic loads on each guide-vane row. This allows a reduction in the vane tangential chord and hence the widening of the free space between blades for the air flowing through the exit stator, Fig. 3. This design reduces the stagnation pressure losses at the exit stator which results in an increase of the turbine efficiency.

The new stator's design methodology is inspired in the design that was numerically and experimentally validated for the guide-vane design of concentric annular rows developed for the self-rectifying biradial air turbine [13], [14].

The current investigation aims to explore the application of this new methodology to the design of axial-flow impulse turbine stators, as first proposed by *Kymaner*. Two types of stators were tested and compared: single row (conventional design) and multiple-rows (new design). Each inlet/exit guide-vane system of the new stator's design comprises three guide-vane rows that produce the required deflection of flow at the rotor inlet while resulting in smaller flow blockage at the downstream guide-vane system. This is expected to significantly reduce the stagnation pressure losses and to improve the turbine efficiency, as compared with the equivalent original design with a single row of guide-vanes, see Fig. 3. A 0.59 m rotor diameter turbine model was constructed and tested at the 55 kW IST variable-flow blow-down test rig under unidirectional steady flow conditions. Experimental results were obtained to assess the performance of the new stator designed for large deflection of the flow at the inlet stator and compare it with the original design.

II. Experimental work

A. Turbine model

The tests were performed with a turbine model rotor diameter $D = 0.59$ m, with hub-to-tip ratio $D_{hub}/D = 0.673$, designed according to the procedure described in detail in [15]. The rotor has $Z = 31$ blades which were made of polyurethane resin using silicone moulds. Figures 4 (a) and (b) show one rotor blade and the rotor blades assembled. The radial gap between the rotor blades and the casing (tip clearance) is less than 1 mm.

Two different stator geometries were tested: 1) a single row of guide-vanes and 2) a set of three-rows of guide-vanes [16]. The tested single-row stator consisted of $Z =$

(a) (b)

Fig. 4. Rotor: (a) blade; (b) assembled rotor.

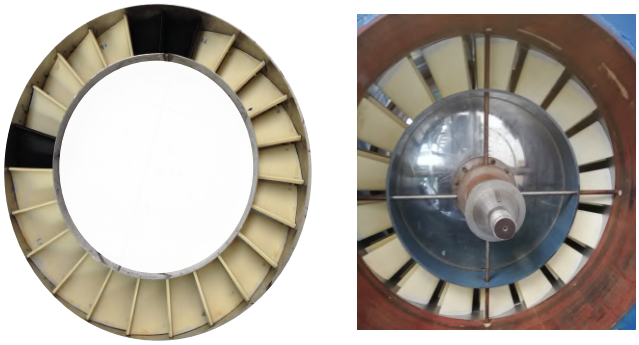

(a) (b)

Fig. 5. High deflection stator geometries tested: (a) single row; (b) set of three-rows of guide-vanes. The black surfaces in photograph (a) are black painted blades.

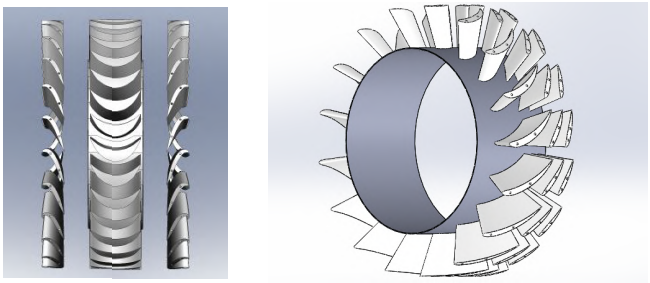

(a) (b)

Fig. 6. Representation of the two stators tested: (a) single row stator on each side of the rotor; (b) geometry of the set of three guide-vane rows.

23 blades; and the other stator had a total of $Z = 51$ blades (17 blades per row), Fig. 5. Both stators were designed for similar high inlet flow turning: $\alpha_1^* - \alpha_2^* = 70\,^\circ$ at the hub varying linearly to $70\,^\circ$ at the shroud, in case of the single row stator, and $\alpha_1^* - \alpha_2^* = 75\,^\circ$ for the set of three guide vane rows.

The available free-space between the three guide-vane rows shown in Fig. 5 (b) is much larger than the one provided by the single row stator, which has vanes with tangential chord-to-pitch ratio larger than unity, Fig. 5 (a). This flow free path through the guide-vanes is associated with the blockage factor ζ, defined as $\zeta = c_\theta/\Delta\Theta$, where c_θ is the tangential chord length of the guide-vanes

TABLE I
ABSOLUTE VELOCITY ANGLE AT THE ENTRY α_1^* AND EXIT α_2^* OF EACH GUIDE-VANE ROW FOR EACH STATOR AND BLOCKAGE FACTOR.

Geometry	Row	α_1^* [°]	α_2^* [°]	ζ [–]
Single row	1	90	17	1.162
Set	1	90	40	0.754
of three	2	42	23	0.748
rows	3	25	15	0.739

at the mean diameter D_m and $\Delta\Theta = \pi D_\mathrm{m}/Z$ is the guide-vane pitch, where Z is the number of guide-vanes in each row. Table I presents for each stator and row the corresponding absolute flow angle at the entry α_1^* and exit α_2^* of each guide-vane row and the corresponding blockage factor ζ.

Due to the three-dimensional shape of the guide-vanes, a 5-axis computer numerical control (CNC) machine was used to manufacture the guide-vane masters, in aluminium AL5083. By the use of silicone moulds, each guide-vane was accurately reproduced using polyurethane resin. Subsequently, the guide-vanes were assembled in two inox steel rolled plates with hub and tip diameter $D_\mathrm{hub} = 0.40\,\mathrm{m}$ and $D_\mathrm{tip} = 0.59\,\mathrm{m}$, respectively. The fixation was made with two M3 type bolts at both ends of each guide-vane. A diffuser with the inlet and outlet diameter ratio $D_\mathrm{in}/D_\mathrm{out} = 0.73$ was assembled between the exit guide-vane set and the plenum chamber.

B. Test rig

The two turbine models were tested at the IST unidirectional 55 kW variable flow test rig, Figs. 7 and 8 [17]. The test rig consists of five main components: (1) electrical generator, (2) turbine model, (3) plenum chamber, (4) Venturi meter and (5) centrifugal fan.

The air enters axially from the atmosphere into the turbine model (2), induced by the suction provided by the centrifugal fan (5). A torque transducer is installed between the turbine and the electrical generator (1), which is connected to the electrical grid through a variable frequency drive that can operate in the four quadrants.

The turbine model is installed upstream of the test-rig plenum chamber (3), which was designed to stabilize the flow before the flow-rate metering. The plenum chamber (3) has a large size, 2.00 m high, 1.40 m long and 0.95 m wide, and so the flow kinetic energy inside the chamber is small. A flow straightener composed of a set of 30 mm diameter plastic tubes is installed upstream of the calibrated Venturi flow-meter (4). The convergent part of the flow-meter is 0.67 m-long and its diameter contracts from 0.80 m to 0.40 m.

C. Instrumentation

The test rig is equipped with instrumentation that provides measurements of differential pressure, rotational speed, torque, atmospheric pressure, dry and wet temperatures.

Pressure taps were installed at the wall of the turbine ducts at four different sections: at inlet of the first set

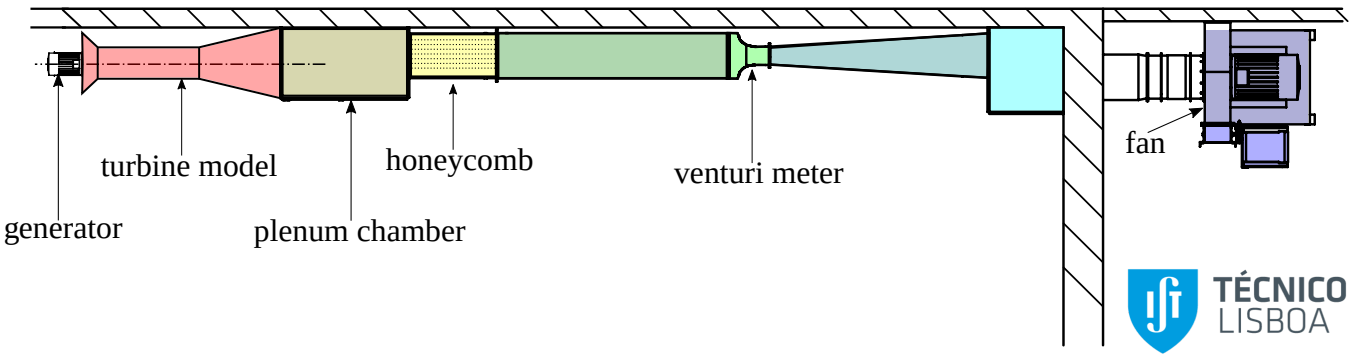

Fig. 7. Schematic representation of a top-view of the IST 55 kW uni-directional turbine test-rig.

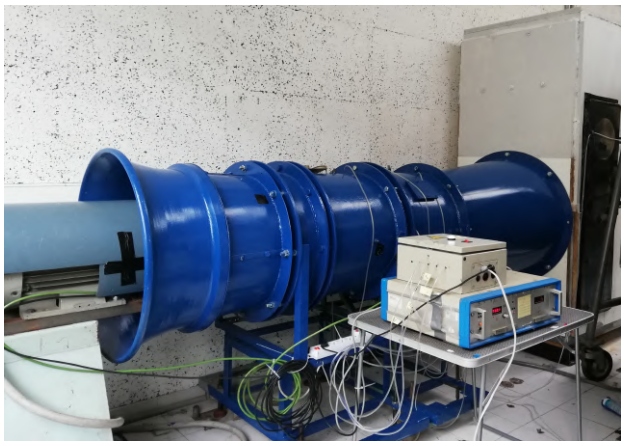

Fig. 8. Turbine model, generator and test rig plenum chamber.

of guide-vanes p_1, at inlet of the rotor p_2, at outlet of the rotor p_3, at inlet of the diffuser p_4, at the wall of the plenum chamber p_5, and at the inlet and at the contraction of the Venturi flow-meter p_6, and p_7, respectively. Differential pressure transducers measured the static pressure relative to the atmospheric pressure at the first five sections. At sections 6 and 7, a differential pressure sensor measured the pressure difference directly at the Venturi flow-meter. For each pressure reading, there were four taps equidistant to a plane normal to the turbine axis. These taps were connected in parallel to obtain the mean pressure at each section. The range of pressure readings was 0−4.2 kPa. All the pressure sensors were calibrated by using a reference pressure transducer of Betz type with an absolute accuracy of 0.05 mm H_2O.

The flow velocity and direction were obtained with a three-hole cylindrical probe, with 6 mm diameter cross-section. The probe was calibrated at the wind tunnel of the IST Turbomachinery Laboratory against one Pitot tube, to characterise its behaviour under different angles and flow Reynolds number.

The turbine shaft torque, T, was measured with a Datum M425 type torque transducer with a range 0 − 20 Nm.

The rotational speed, Ω, was measured with a photo-electric speed transducer (inserted into the torque transducer) which emits a pulse when the toothed wheel passes over. The calibration was executed during the tests with a tachometer (with an absolute accuracy of 0.05 r.p.m.).

The volume flow rate, Q, was determined by measuring the pressure drop in the pre-calibrated Venturi flow-meter.

The atmospheric pressure and dry temperature were measured with a digital manometer Testo model 511 with a precision of ±300 Pa and a digital thermometer Testo, type 175 H1, with an accuracy of ±0.1 ºC, respectively. The wet-bulb temperature was read by a mercury thermometer covered in water-soaked cloth over which the atmospheric air is passed. This mercury thermometer has an accuracy of 0.5 mmHg. The density of the air at the turbine inlet is then given by Air Moving and Conditioning Association (AMCA) standard 210/67, [18], Eq. (1).

$$\rho = \frac{p_{\text{atm}} - 0.378 \times p_{\text{p}}}{R(T_{\text{dry}} + 273.15)}, \tag{1}$$

where

$$p_{\text{p}} = p_{\text{e}} - p_{\text{atm}} \frac{T_{\text{dry}} - T_{\text{wet}}}{1500}, \tag{2}$$

and

$$p_{\text{e}} = 3.25 \times {T_{\text{dry}}}^2 + 18.6 \times T_{\text{wet}} + 692. \tag{3}$$

Here, p_{atm}, p_{p} and p_{e} are in Pa; T_{dry} and T_{wet} are in ºC; $R = 287.1$ J/ kgK; and ρ is in kg/ m^3.

III. Experimental results

The experimental results presented in this section refer to the two different turbine models, one equipped a single row of $Z = 23$ guide-vanes designed for a rotor inlet absolute flow of $\alpha_2 = 20\,^\circ$ at the hub and $17\,^\circ$ at the shroud, and another one with three rows of $Z = 3 \times 17$ guide-vanes designed for a rotor inlet absolute flow of $\alpha_2 = 15\,^\circ$. The tests were performed with both inlet and outlet stators placed at 100 mm upstream and downstream of the rotor. The performance of the two turbine models was evaluated through the following dimensionless variables: the power coefficient

$$\Pi = \frac{P}{\rho \Omega^3 D^5}, \tag{4}$$

the pressure coefficient

$$\Psi = \frac{\Delta p_0}{\rho \Omega^2 D^2}, \tag{5}$$

the flow-rate coefficient

$$\Phi = \frac{Q}{\Omega D^3} \tag{6}$$

and the total-to-static efficiency

$$\eta_{\text{ts}} = \frac{\Pi}{\Psi\Phi}. \tag{7}$$

Here Ω is the rotational speed (radians per unit time), Δp_0 the pressure head between the atmosphere and the plenum chamber, D the turbine rotor diameter and $P = T\Omega$, is the turbine power output, where T is the shaft torque. The bearings mechanical losses were measured separately and added to the torque T measured during the tests.

The experimental results were obtained for a range of values of the flow-rate coefficient Φ, and of the rotational speed Ω, corresponding to Reynolds number, $\text{Re} = \rho\Omega D^2/\mu$ (μ is the air viscosity), as shown in Table II for both tested stators.

The evolution of the efficiency, power and pressure coefficients as functions of the flow coefficient, for the single row and the three-row stator turbine models, without the downstream stator, are represented in Figs. 9, 10 and 11.

Results in Fig. 9 show that the maximum efficiency of the turbine model without the downstream stator, equipped with a single row of guide-vanes and with the system of three rows of guide-vanes is $\eta_{\text{ts}} = 0.67$ for $\Phi = 0.12$ and $\eta_{\text{ts}} = 0.63$ for $\Phi = 0.11$, respectively. Both efficiency peaks are very modest when compared with the results in references [9]–[11].

Results in Figs. 10 and 11 reveal that the power and pressure coefficients are higher for the turbine model with the set of three rows of guide vanes, which has a slightly larger angular momentum at the rotor inlet.

The evolution of the total-to-static efficiency and the pressure coefficient as functions of the flow coefficient are represented in Figs. 12 and 13, for both complete turbine models, with upstream and downstream guide-vanes.

Results in Fig. 12 show that the maximum efficiency achieved by the turbine model equipped with a single row of guide-vanes and with the system of three rows of guide-vanes is $\eta_{\text{ts}} = 0.23$ for $\Phi = 0.13$ and $\eta_{\text{ts}} = 0.33$ for $\Phi = 0.12$, respectively.

Data illustrated in Fig. 13 demonstrates that the pressure coefficient is significantly higher for the turbine model with the traditional single-row stator. This result was expected, since the new geometry allows an increase in the flow passage area and thus a decrease in the stagnation pressure losses, which provide a decrease in the pressure head when compared with the stator with a single row.

TABLE II
RANGES OF Ω, Re AND Φ STUDIED.

Geometry	Ω[r.p.m.]	Re[–]	Φ[–]
Single row	400 – 800	9.6×10^5 1.9×10^6	0.05 – 0.20
Three rows	400 – 800	9.6×10^5 1.9×10^6	0.05 – 0.19

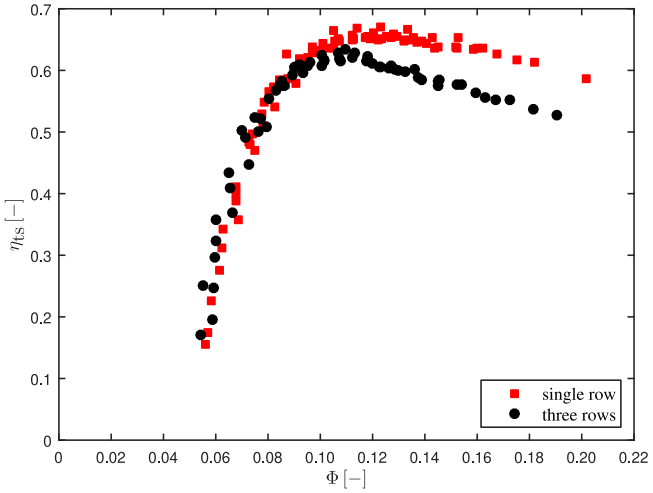

Fig. 9. Efficiency versus the flow-rate coefficient of the axial-flow impulse turbine model equipped with a single row of guide-vanes and with the system of three-row guide-vanes, without the downstream stator.

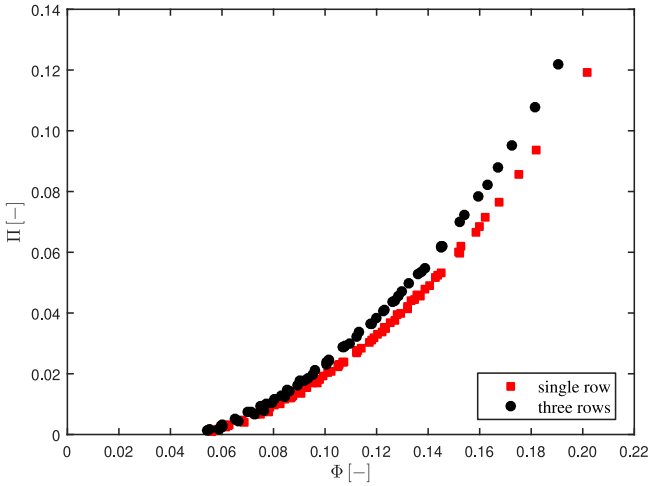

Fig. 10. Power coefficient versus the flow-rate coefficient of the axial-flow impulse turbine model equipped with a single row of guide-vanes and with the set of three rows of guide-vanes, without the downstream stator.

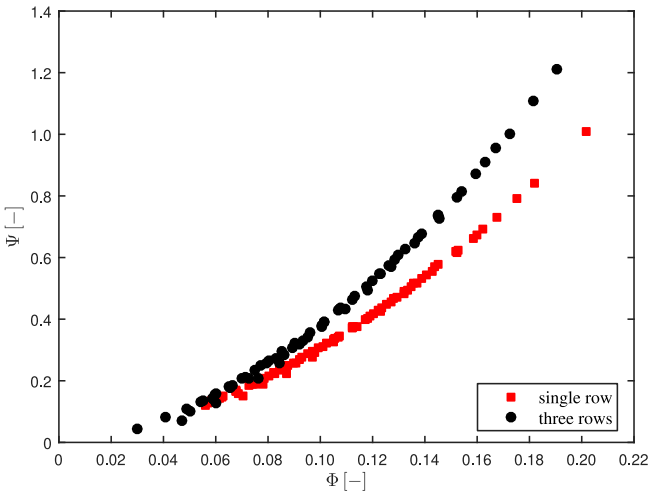

Fig. 11. Pressure coefficient versus the flow-rate coefficient of the axial-flow impulse turbine model equipped with a single row of guide-vanes and with the set of three rows of guide-vanes, without the downstream stator.

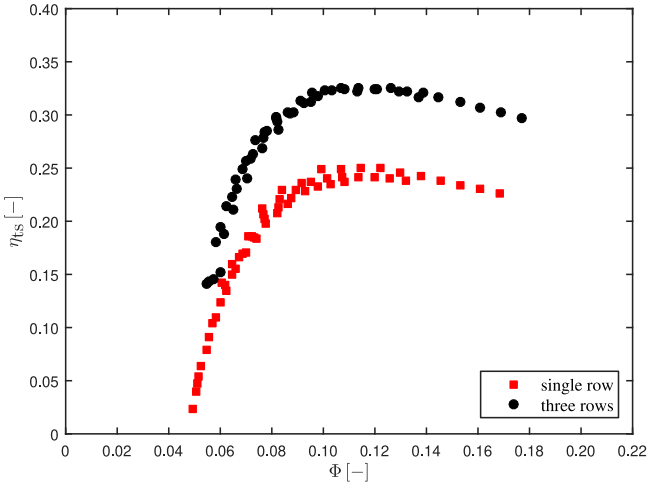

Fig. 12. Efficiency versus the flow-rate coefficient of the complete axial-flow impulse turbine model equipped with a single row of guide-vanes and with the system of three rows of guide-vanes the rotor.

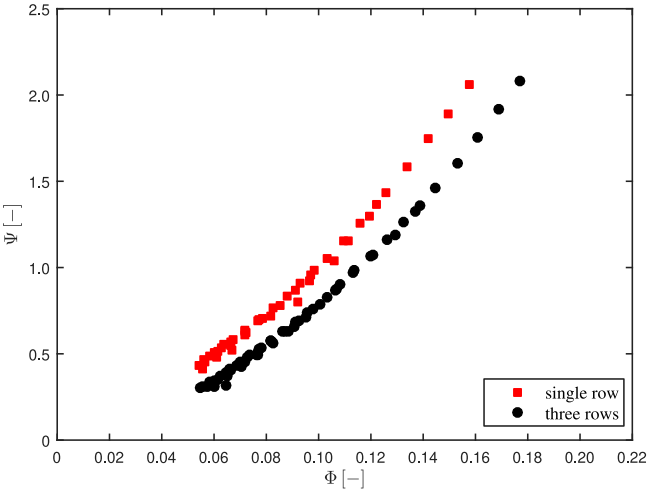

Fig. 13. Pressure coefficient versus the flow-rate coefficient of the complete axial-flow impulse turbine model equipped with a single row of guide-vanes and with the set of three rows of guide-vanes.

Traversing tests were executed with a directional probe, for four flow-rate coefficients in the case of the conventional stator and six for the stator with new geometry, in order to find the flow angle, dynamic and total pressure at the rotor inlet (exit of the stator). These tests were made along the vane span h, with a discretisation in the radial direction $\Delta r = 1\,\text{mm}$, for $Z\theta/(2\pi) = 0, 0.39, 0.78, 1$ along the blade pitch, $\Theta_{\text{pitch}} = 2\pi/Z$, for the stator with single row, and $Z\theta/(2\pi) = 0.06, 0.27, 0.55, 0.83, 1$ for the stator with three rows. Detailed information is presented in Tab. III.

Figure 14 shows the radial distribution of the absolute flow angle at the rotor inlet as a function of the non-dimensional radial position $r^* = (2r - D_{hub})/(D - D_{hub})$, where r is the radial position of the measurement, for $\Phi = 0.14$ and $Z\theta/(2\pi) = 1$. Note that $r^* = 0$ at the hub and $r^* = 1$ at the shroud. It can be seen that both geometries are in conformity with the numerical design (see section II-A).

TABLE III
DETAILED INFORMATION ABOUT THE DETERMINATION OF VELOCITY FIELD AT THE ROTOR INLET.

Geometry	h[mm]	Δr[mm]	Θ_{pitch} [rad]
Single row	91.5	1	0.273
Three rows	91.5	1	0.370

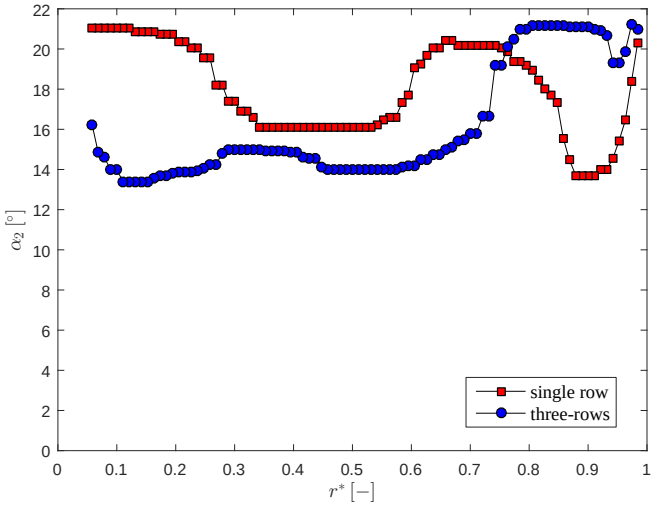

Fig. 14. Radial distribution of the absolute flow angle α_2 measured at the rotor inlet for both stators, for $\Phi = 0.14$.

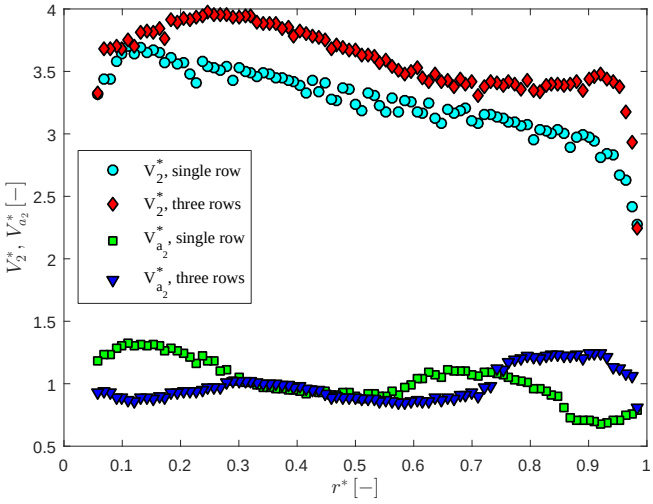

Fig. 15. Radial distribution of the non-dimensional axial component of the absolute flow axial velocity and the non-dimensional absolute velocity at the rotor inlet for both stators.

The mean absolute flow angle measured at the exit of the set of three guide-vane rows is $\overline{\alpha}_2 = 15.7\,°$, which is very close to the design value $\overline{\alpha}_2^* = 15\,°$. The corresponding value for the single guide-vane row is $\overline{\alpha}_2 = 18.4\,°$, which lies inside the design range of flow angles at the rotor inlet, between the hub and the shroud, $17\,° \leq \alpha_2^* \leq 20\,°$.

The non-dimensional absolute axial velocity component ${V_{a_2}}^* = V_{a_2}/\overline{V}_{a_2}$ and the non-dimensional absolute velocity ${V_2}^* = V_2/\overline{V}_{a_2}$ are plotted in Fig. 15 versus the non-dimensional radial position r^*, for $\Phi = 0.14$ and $Z\theta/(2\pi) = 1$, where $\overline{V}_{a_2}$ is the average axial component of the absolute velocity. As expected from the previous results, the non-dimensional absolute velocity is slightly larger for the case of the three-rows arrangement, since the angle of deflection of the guide-vanes is slightly

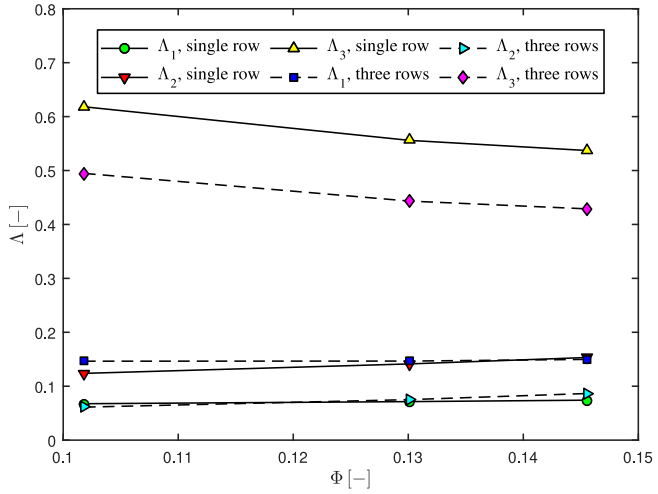

Fig. 16. Non-dimensional stagnation pressure losses versus flow-rate coefficient, for both geometries.

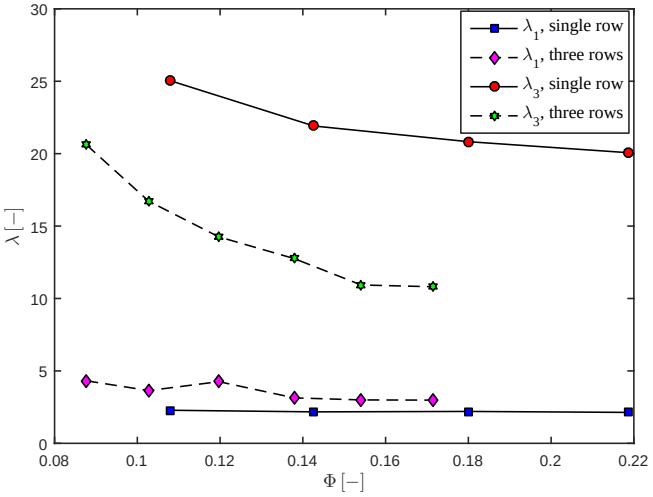

Fig. 17. Values of λ_1 and λ_2 versus Φ, for both configurations.

higher. It can also be seen that its distribution is similar for both stators.

In order to evaluate the flow losses along the turbine, we define the dimensionless stagnation pressure loss, Λ_i. These coefficients were calculated for three sections: (1) inlet stator Λ_1; (2) rotor Λ_2 and (3) exit stator Λ_3. They are defined as

$$\Lambda_1 = \frac{(p_\mathrm{A} - \overline{p}_{0_2})}{\Delta p_0}, \tag{8}$$

$$\Lambda_2 = \frac{Q(\overline{p}_{0_2} - \overline{p}_{0_3}) - T\Omega}{Q\Delta p_0}, \tag{9}$$

$$\Lambda_3 = \frac{(\overline{p}_{0_3} - \Delta p_0)}{\Delta p_0}, \tag{10}$$

where $\overline{p}_{0_2}$ and $\overline{p}_{0_3}$ are the averaged stagnation pressure at inlet and exit of the rotor and p_A is the atmospheric pressure. Note that $\Delta p_0 = p_\mathrm{A} - p_\mathrm{B}$, where p_B is the averaged stagnation pressure at the plenum chamber, and $\sum_{i=1}^{3} \Lambda_i + \eta_\mathrm{ts} = 1$, where $i = 1, 2, 3$ identifies the turbine part number. Figure 16 illustrates the distribution of the non-dimensional stagnation pressure losses for both turbine models.

Results presented in Fig. 16 reveal three main aspects:

1) Although it is relatively small, Λ_1 is 48% higher for the stator with three rows when compared with the conventional single-row geometry. This difference is due to the flow deflection through three guide-vane rows, instead of a single one, which results in larger stagnation pressure losses.
2) Λ_2 is similar for both stators. The slight difference may be related to the incident losses caused by the single-row system, that implies larger non-dimensional stagnation pressure losses.
3) Λ_3 is 80% lower for the new stator geometry, which explains the larger turbine efficiency achieved by this turbine model. The large solidity ratio of the single-row stator (which exceeds 1) produces significantly higher stagnation pressure losses at the downstream stator, as compared with the three-guide-vane-row stator.

Another way to characterize the losses at the stators upstream and downstream of the rotor is through the guide-vane loss coefficients, which are defined as

$$\lambda_1 = \frac{p_\mathrm{A} - \overline{p}_{0_2}}{\frac{1}{2}\rho \overline{V}_{\mathrm{a}_2}^{\,2}}, \tag{11}$$

$$\lambda_3 = \frac{\overline{p}_{0_3} - p_B}{\frac{1}{2}\rho \overline{V}_{\mathrm{a}_3}^{\,2}}, \tag{12}$$

where λ_1 refers to the stator upstream the rotor and λ_3 to the stator downstream the rotor.

Values of λ_1 and λ_3 are plotted, for both stators, in Fig. 17, versus the flow rate coefficient. It may be seen that λ_1 and λ_2 decrease with increasing flow rate coefficient Φ, due to the influence of the Reynolds number. As can be observed in Fig. 16, the guide-vane loss coefficient at the upstream stator with three rows is also slightly higher when compared with the single-row one, for the reasons mentioned before. The coefficients λ_1 and λ_2 become approximately constant for the larger values of Φ. Considering only the two last values of λ for each guide-vane system, we have $\lambda_3 \simeq 10.9$ for the three-row stator and $\lambda_3 \simeq 20.4$ for the single-row stator. This shows that the three rows of guide-vanes provided a pressure loss reduction of 51%, when compared with the single-row stator.

The rotor total-to-total efficiency is defined as

$$\eta_{\mathrm{tt}_\mathrm{rotor}} = \frac{T\Omega}{(\overline{p}_{0_2} - \overline{p}_{0_3})Q}\,. \tag{13}$$

Figure 18 shows a plot of the rotor total-to-total efficiency for different values of the non-dimensional flow-rate coefficient.

The rotor peak efficiency is $\eta_{\mathrm{tt}_\mathrm{rotor}} = 0.71$ (for $\Phi = 0.12$). This may be regarded as a very modest value for a rotor that is largely identical to a rotor of a conventional axial-flow impulse turbine. This low value of $\eta_{\mathrm{tt}_\mathrm{rotor}}$ explains the low efficiency of the tested turbine models. In fact, in spite of the new stator geometry effectively providing higher efficiency when compared with the traditional single-row stator, the maximum turbine efficiency is lower than the values of efficiency

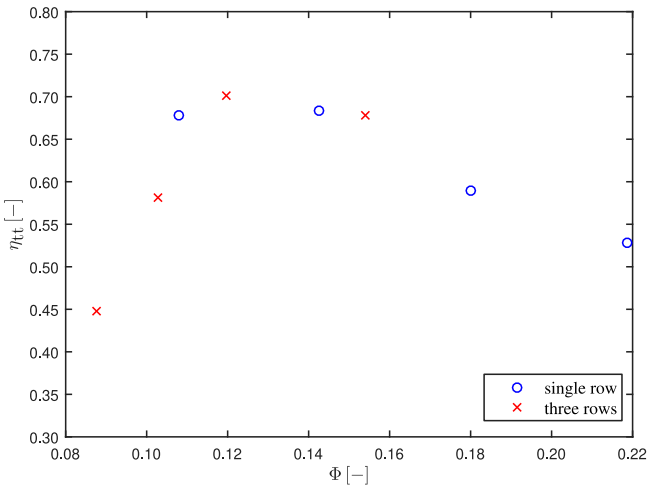

Fig. 18. Rotor total-to-total efficiency versus Φ.

reported in previous investigations [9]–[11] characterized by a smaller flow-deflection at the inlet guide-vanes.

IV. Conclusions

Two stators configurations for a self-rectifying axial-flow air turbine were presented and tested under unidirectional flow at the IST 55 kW test rig: the conventional design with a single row of guide-vanes and the new design with three-rows of guide-vanes. Both stators were designed to produce identical angular flow-deflection. The three-row guide-vane system allows a considerably smaller flow blockage, and consequently a significant reduction in the stagnation pressure loss, at the exit stator. In fact, this is the main objective underlying the new design: an improvement of the turbine efficiency in bi-directional flow.

The measured peak efficiency is $\eta_{ts} = 0.23$ at $\Phi = 0.13$ for the conventional single-row stator, and $\eta_{ts} = 0.33$ for $\Phi = 0.12$, for the new design with three rows of guide-vane. Although these peak-efficiency values are modest, their comparison shows that the three-row stator allows an increase of 43% in turbine peak efficiency, as compared with the single-row stator configuration.

It should also be noted that the flow angles measured at the inlet of the rotor are close to the ones expected from the design: $\overline{\alpha}_2 = 15.7\,^\circ$ for the three-row stator and $\overline{\alpha}_2 = 18.4\,^\circ$ for the single row.

The stagnation pressure losses at the exit of the rotor were 80% lower for the new geometry. However, the turbine peak efficiency is 48% lower than achieved in previous investigations with other self-rectifying axial-flow impulse turbines (see [9]–[11]). The modest efficiency of the rotor (peak value $\eta_{tt_{rotor}} = 0.71$) very negatively affects the whole turbine performance. This suggests that the rotor should be redesigned

The peak efficiency for the turbine model without the downstream guide vanes is $\eta_{ts} = 0.63$, for the new three-row stator geometry and $\eta_{ts} = 0.67$ for the single-row stator.

Finally, the concept of using multiple guide-vane rows to achieve high deflection at low solidity ratio, and therefore high turbine shaft torque and lower stagnation pressure losses at the exit of the rotor, is seen to be a promising way to increase the efficiency of self-rectifying axial-flow impulse turbines.

Acknowledgement

This work was supported by FCT, through IDMEC, under LAETA, project UID/EMS/50022/2019. The fourth author was supported by FCT researcher grant No. IF/01457/2014.

References

[1] S. S. Prakash, K. A. Mamun, F. R. Islam, R. Mudliar, C. Pau'u, M. Kolivuso, and S. Cadralala. Wave energy converter: A review of wave energy conversion technology. In *Proceedings of the 3rd Asia-Pacific World Congress on Computer Science and Engineering (APWC on CSE)*, pages 71–77, Dec 2016.

[2] A. F. O. Falcão. Wave energy utilization: A review of the technologies. *Renewable and Sustainable Energy Reviews*, 14(3):899 – 918, 2010.

[3] R. Starzmann and T. Carolus. Model-based selection of full-scale Wells turbines for ocean wave energy conversion and prediction of their aerodynamic and acoustic performances. *Proc Inst Mech Eng Part A: J Power Energy*, 228:2–16, 2014.

[4] R. Curran and L. M. C. Gato. The energy conversion performance of several types of Wells turbine designs. *Proc Inst Mech Eng, Part A: J Power and Energy*, 211(2):133–145, 1997.

[5] K. Mala, S.N. Badrinath, S. Chidanand, G. Kailash, and V. Jayashankar. Analysis of power modules in the Indian wave energy plant. In *2009 Annual IEEE India Conf*, pages 1–4, Dec 2009.

[6] J.A. Rea, J.F. Kelly, R. Alcorn, and D. O'Sullivan. Development and operation of a power take off rig for ocean energy research and testing. *Proc 9th European Wave and Tidal Conf, Southampton, UK*, 2011.

[7] R. Alcorn, A. Blavette, M. Healy, and A. Lewis. FP7 EU funded CORES wave energy project: a coordinators' perspective on the Galway Bay sea trials. *Underwater Technology*, 2014.

[8] F. Thiebaut, D.O. Sullivan, P. Kracht, S. Ceballos, J. López, C. Boake, J. Bard, N. Brinquete, J. Varandas, L.M.C. Gato, R. Alcorn, and A.W. Lewis. Testing of a floating OWC device with movable guide vane impulse turbine power take-off. In *Proc 9th European Wave and Tidal Energy Conf*, 2011.

[9] T. Setoguchi, M. Takao, S. Santhakumar, and K. Kaneko. Study of an impulse turbine for wave power conversion: effects of Reynolds number and hub-to-tip ratio on performance. *Journal of Offshore Mechanics and Artic Engineering*, 126:137–40, 2004.

[10] A. Thakker, H. B. Khaleeq, M. Takao, and T. Setoguchi. Effects of hub-to-tip ratio and Reynolds number on the performance of impulse turbine for wave energy power plant. *KSMW International Journal*, 17(11):1767–1774, 2003.

[11] L. Zhen, C. Ying, L. Ming, and S. Hongda. Steady state performance of an axial impulse turbine for oscillating water column wave energy converters. *Energy*, 141:1–10, 2017.

[12] L. Trigo. The OWC option. In *Workshop on Powering the Future? Marine Energy Oportunities, Lisbon*, 2009.

[13] A. R. Maduro, L. M. C. Gato, J. C. C. Henriques, and D. N. Ferreira. Design and optimization of fixed guide vanes arranged into concentric annular rows for a self-rectifying biradial air-turbine. In *Proc 12th European Wave Tidal Energy Conf, Cork, Ireland*, 2017.

[14] A. A. D. Carrelhas, A. R. Maduro, L. M. C. Gato, J. C. C. Henriques, and A. F. O. Falcão. Performance of the self-rectifying biradial air turbine with fixed guide vanes arranged into concentric annular rows. In *Proc 12th European Wave Tidal Energy Conf, Cork, Ireland*, 2017.

[15] R. P. F. Gomes, J. C. C. Henriques, L. M. C. Gato, and A. F. O. Falcão. Multi-point aerodynamic optimization of the rotor blade sections of an axial-flow impulse air turbine for wave energy conversion. *Energy*, 45(1):570–580, 2012.

[16] J. Nunes. Development of a new design methodology of axial-flow impulse turbine stators. Technical report, LAETA, IDMEC, Instituto Superior Técnico, Universidade de Lisboa, 2018.

[17] F. X. Correia da Fonseca, J. C. C. Henriques, L. M. C. Gato, and A. F. O. Falcão. Oscillating flow rig for air turbine testing. *Renewable Energy*, 142:373–382, 2019.

[18] Air Movement and Control Association International Inc. *Laboratory Methods of Testing Fans for Aerodynamic Performance Rating*, 1999.